Nonlinear Performance Limits for High Energy Density Piezoelectric Bending Actuators*

Robert J. Wood, Erik Steltz, and Ronald S. Fearing
Department of Electrical Engineering and Computer Science
University of California at Berkeley
Berkeley, California, USA
{*rjwood ees132 ronf*}*@eecs.berkeley.edu*

***Abstract*— To keep pace with recent advances in microrobotic structures demands actuator technologies which can deliver high power and precise motion. For electroactive material based actuators, high power typically implies either high field or high current drives which may lead to greater nonlinearities such as saturation, softening, and increased loss. Physical modeling of actuators is normally taken to be linear since the range of displacements, applied loads, and applied fields is typically small. If extrapolated to high drive conditions, these linear models significantly over predict the power which can be delivered. For actuators driving dynamic systems, a complete nonlinear model of the system will improve controllability and give more accurate estimations of power delivery capabilities. Here static nonlinearities and dynamic linear and nonlinear parameters are derived for high performance piezoelectric bending actuators.**

***Index Terms*— piezoelectric actuators, creep, saturation, nonlinear modeling, microactuators**

I. Introduction

There have been various approaches to formulating the static constitutive equations of piezoelectric bending actuators. Examples of these include Weinberg [22] and Smits [18] who used energy methods, DeVoe [7] modeled multilayered actuators, and Wang [20] described the performance of bimorphs with a central layer. There have also been descriptions of the dynamic response of such actuators as by Goldfarb [9], [11], and Sitti [17], as well as the inherent nonlinearities of piezoelectric materials under high applied fields such as in Wang [21].

Wood, et al [25] described the design and static linear modeling of high energy density piezoelectric bending actuators by utilizing laminate plate theory. These actuators achieve their high performance through intrinsic and extrinsic geometric improvements that uniformly distribute the actuator strain along its length thereby maximizing the total strain energy at fracture. High field driving techniques were presented in [25] which greatly increase static bimorph actuator performance, however these results do not scale linearly with changes in field. The high fields described in [25] reach a maximum of approximately $2.5\mathrm{V}\mu\mathrm{m}^{-1}$ where commercially available specifications are typically lower ($0.5\mathrm{V}\mu\mathrm{m}^{-1}$ from Piezo Systems, Inc.). Intrinsic nonlinearities that arise from high field drive of piezoelectric ceramics are modeled here through least squares fitting of empirical data. The effect geometric changes have on the dynamic properties of the actuator is nontrivial and are derived here as part of a full nonlinear model of such actuators. Because of the field effects on the dynamic properties, the ultimate power delivery capability of piezoelectric actuators is greatly reduced. Piezoceramic softening and increased loss at high fields cause dissipation to occur withing the actuator, which creates significant divergence between static linear predictions and actual performance.

The modeling and results from this paper are specific to the morphology of the particular actuators used, however, the methods used apply to a number of transducers, both precision and power. Moreover, they examine a collection of phenomena inherent to piezoelectric materials and ways of describing them. First, three phenomena are investigated: creep, saturation and hysteresis, and stress effects. Finally, the conservative and nonconservative parameters are determined for use in a complete dynamic model. Of these, field effects on actuator softening and losses are examined. The models presented here encompass any piezoelectric bending actuator regardless of material makeup, geometry, anisotropies, and ply layup.

A. Materials and Methods

The transducers in question are custom made bimorph clamped-free bending (d_{31} mode) actuators. These devices were designed for optimal energy density as described in [25] for use in microrobotics projects, specifically for flapping wing micro air vehicles (MAV) [2], [3], [23].

1) Actuator Construction: The actuator design is shown in Fig. 1. The two geometric improvements to the actuator consist of a rigid extension [4] and variable width tapering [25]. Adding a rigid extension not only gives the ability to tailor kinematic properties, but also improves the energy density by a maximum of 33% by acting as a lever arm to more uniformly distribute the external moment along the length of the beam. By tapering the width (while constraining the planform area to be constant), the strain can be uniformly distributed along the actuator which yields a 33% increase in energy density. The actuators are constructed from commercially available PZT-5H plates, laser micromachined to desired geometries. Passive layers consist of composites: S2-glass for the extension and ultra high modulus (UHM) carbon fiber for the actuator elastic layers. Both are prepregs (preimpregnated with a catalyzed,

*This work is partially supported by ONR MURI N00014-98-1-0671, DARPA, and NSF IIS-0083472

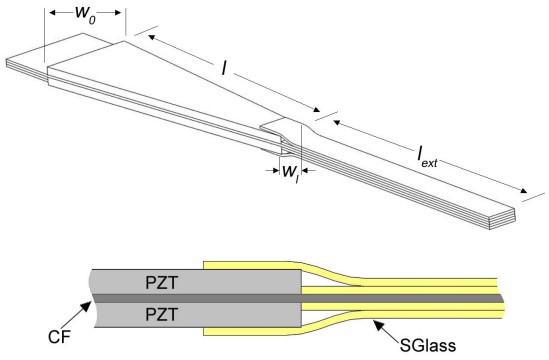

Fig. 1. Bimorph drawings with (a) pertinent dimensions and (b) cross section showing layup.

uncured epoxy resin) and are also laser micromachined, layed up with the ceramic, and cured under vacuum. The actuators used in this study are a total of 10mm long, and weigh approximately 12mg. Along with the geometric modifications, a novel drive method was developed which allows PZT plates to have high fields applied without the risk of depolarization. This drive method grounds one outer surface of the bimorph, applies a static bias voltage V_b to the other, and the center electrode is driven from $V_b/2$ to $\pm V_b/2$. Thus no plate is ever reverse biased with respect to its polling direction. The convention used in this work calls $V_b/2$ applied to the center electrode the neutral actuator position. A brief overview of the static actuator performance derivations is given in appendix A.

2) Position Sensors: To characterize the behavior of the actuators, a real time measure of tip position is desired. Because of small actuator motions ($< 500\mu$m) and small form factor, commercially available displacement sensors are not feasible and thus custom made versions are used. Initially, strain gages (either externally mounted [24] or using the PZT surface itself [4]) were used to monitor curvature and therefore determine actuator tip position. However, difficulty in wiring and questions of nonlinearities on the surface of the PZT (i.e. hysteresis) led to a search for a non-contact position sensor.

Custom reflective position sensors were created [19] utilizing a side view fiber optic to sense the actuator position. The sensors operate by reflecting light off the actuator tip and receiving the reflected signal. For increased sensitivity the light signal was amplitude modulated and then demodulated in analog circuitry.

The custom position sensors and associated analog circuitry are experimentally accurate to approximately 3.7 μm of actuator deflection and have a bandwidth of 3700Hz. However, the dynamics of the processing circuitry were characterized; processing data off line leads to a bandwidth increase to approximately 10kHz. The only actuator modification the sensors require is to enhance the reflectivity of the tip of the extension.

II. Static Nonlinearity Modeling

Piezoelectric transducers are used in a number of scenarios in which either precise position control or high bandwidth sensing and actuation is desired. Certain inherent material properties cause piezoceramics to exhibit a viscoelastic response and cause saturation with high applied fields.

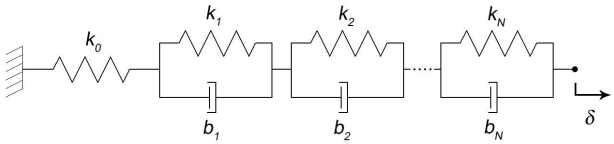

Fig. 2. Generalized Kelvin-Voigt model for viscoelastic materials.

A. Creep

Creep is a phenomenon which appears in the voltage-displacement characteristics of piezoelectric ceramics as a viscoelastic material property. The presence of creep can cause substantial errors for precision positioning actuators, or could affect the dynamics of power actuators. Creep exists in both the electrical and mechanical domains, however it is modeled by a series connection of parallel spring damper elements collectively called the generalized Kelvin-Voigt model and is shown in Fig. 2. This model for viscoelastic materials is similar to those in [12], [16]. As the number of elements N is increased, the accuracy of the fit to creep data is improved, however each additional spring damper element increases the order of the model. The displacement $\delta(t)$ for the system in Fig. 2 is derived as follows:

$$\delta(t) = F_0 u(t) \left[\frac{1}{k_0} + \sum_{n=1}^{N} \frac{1}{k_n} \left(1 - e^{-\frac{t}{\tau_n}} \right) \right], \quad (1)$$

where $\tau_n = b_n/k_n$, F_0 is the static internally applied stress from the piezoelectric effect, and $u(t)$ is the unit step. Ideally, creep would be observed by applying a static field and measuring the displacement for $t > 0$. This is not practical for the case of a bending actuator however since the Q is typically high so that such a test will cause mechanical failure. Instead, the applied field was ramped slowly to a set value (in this case $0.5V\mu\text{m}^{-1}$), but done so such that the ramp time was significantly lower than $\min(\tau_n)$ (for this test, the ramp was completed in 0.2s) to mimic a step input. Finally, the steady state field value was kept small so as to eliminate the effects of high field displacement saturation as in [6]. A nonlinear least squares regression fitting of this measured displacement to the model parameters in Fig. 2 was done for various model orders and is shown in Fig. 3. Note that this is done for one set field value. It is assumed that this will not scale with increasing field because of softening and other effects discussed later.

B. Saturation

Displacement-voltage saturation is always present for piezoelectric ceramics operating at high fields. This is due to the finite strain available through domain reorientation. The model for saturation is analogous to the Kelvin-Voigt model for creep but is instead a number of parallel series

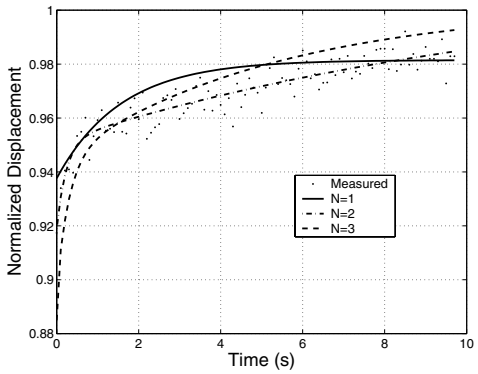

Fig. 3. Creep data with fit to Kelvin-Voigt models of increasing order.

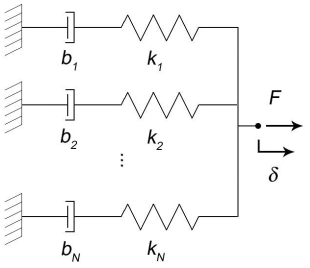

Fig. 4. Maxwell Slip model for actuator saturation.

of spring dampers called the Maxwell Slip model similar to that in [9] (and similar to the Prandtl-Ishlinskii operator and the Preisach Hysteresis model [6]) and is shown in Fig. 4. The dampers in the above model are not viscous, but instead are analogous to Coulomb friction in which a break away force f^b must be overcome to achieve any motion. Since the elements are in parallel, the forces add as follows:

$$F = \sum_{n\in\Omega} k_n \left(\delta - \delta_n^d\right) + \sum_{m\in\Psi} f_m^b \operatorname{sgn}\left(\dot{\delta}\right), \qquad (2)$$

where the individual damper positions are defined as:

$$\left[\delta^d\right] = \begin{cases} \delta_i^d : i \in \Omega \\ \delta - \frac{f_j^b}{k_j} \operatorname{sgn}\left(\dot{\delta}\right) : j \in \Psi \end{cases}, \qquad (3)$$

where in the above two equations the sets Ω and Ψ are defined to be $\Omega = \left\{i : \left|k_i\left(\delta - \delta_i^d\right)\right| < f_i^b\right\}$ and $\Psi = \left\{j : \left|k_j\left(\delta - \delta_j^d\right)\right| \geq f_j^b\right\}$. Note that the sum of the sizes of the two sets must equal N, the number of Maxwell Slip elements. An experimentally measured hysteresis curve is shown in Fig. 5 along with the model fit.

C. Stress based effects

Finally, it is desired to discover if the displacement properties of the actuator change with increased external loading. This is done by again performing hysteresis tests, however in this case static loads are isotonically applied to the actuator with a fixed mass. For the case of the actuator in question, the loads chosen are of the order of the maximum loading expected during use (0, 50, and 100mN). The actuator is brought to the neutral position, the load is applied, and the field is ramped from 0 to

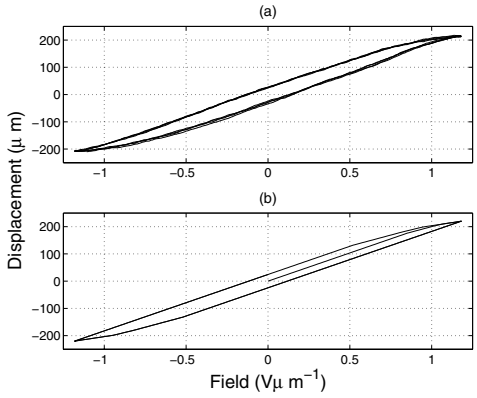

Fig. 5. Measured hysteresis (a) and fit to Maxwell Slip model (b).

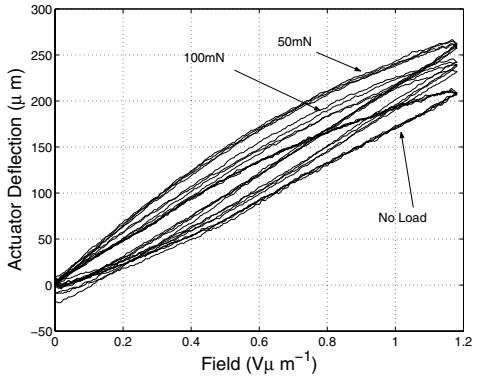

Fig. 6. Work loop for various applied static loads.

$E_{3,\max}$ for a number of cycles while observing the tip displacement. If there is stress based saturation or softening of the piezoelectric material, the displacement magnitude will decrease with increasing external loading. For a linear actuator, the motion will remain the same for any arbitrary loading, thus any stress based effects will appear as another nonlinearity. The hysteresis loops for the three loads are shown in Fig. 6. What is interesting from these results is that there is no saturation, however there is a slight inverse effect. Note that the magnitude of the displacement with an applied load is greater than that with no load (with a peak at 50mN for saturation reasons not discussed here). This is easily explained by the presence of stress based d_{31} enhancement. It has been shown [1], [13], [26], [27] that compressive stress on PZT degrades the piezoelectric coupling coefficients while tensile stress causes an enhancement. Applying a load to the distal end of a bimorph actuator puts the PZT plate which is doing work on the load in tension, causing the above phenomena.

III. Linear and Nonlinear Conservative Parameter Modeling

Wood [25] described how the quasi-static performance and stiffness of an actuator will vary with extension length and degree of tapering for a given field. Here, the remaining dynamic parameters are derived. The mechanical model used to describe the actuator dynamic performance is shown in Fig. 7.

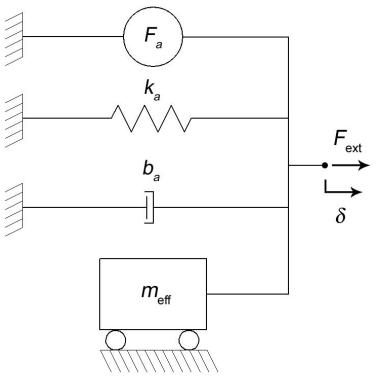

Fig. 7. Mechanical model of actuator.

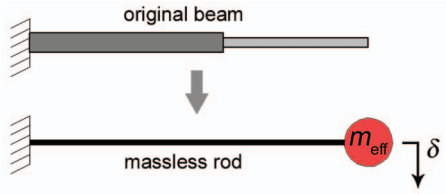

Fig. 8. Model for calculating the effective mass of a cantilever.

A. *Effective Cantilever Mass*

The mass of a cantilever as represented by the mass in the system in Fig. 7 is termed the effective mass, m_{eff}. This quantity is determined by calculating the kinetic energy of a massless rod with a point mass at the distal end (shown in Fig. 8) and equating this to the sum of each particle in the beam. The kinetic energy of an oscillating point mass at the distal and of a massless rod is given by the following:

$$T = \frac{1}{2} m_{\text{eff}} \dot{\delta}(l)^2 . \tag{4}$$

Equating the sum distributed kinetic energy of a cantilever beam is as follows:

$$T = \frac{1}{2} w t \rho \int_0^l \dot{\delta}(x)^2 \, dx, \tag{5}$$

where w, t, and ρ are the width, thickness, and density of the beam respectively. Rearranging the terms in (4) and (5) and solving for m_{eff} for a homogeneous rectangular beam gives,

$$m_{\text{eff}} = m_{\text{beam}} \frac{\int_0^l \dot{\delta}(x)^2 \, dx}{l \dot{\delta}(l)^2}, \tag{6}$$

where m_{beam} is the gross beam mass defined as $wtl\rho$. This can be rewritten to accentuate the mass multiplier $M(\cdot)$ as follows: $m_{\text{eff}} = M(\cdot) m_{\text{beam}}$. For a rectangular beam with a point load, the term $\delta(x)$ is given in appendix B. Substituting this into (6) yields the classic result for a straight cantilever beam, $m_{\text{eff}} = (33/140) m_{\text{beam}}$. This gets to be more difficult when considering beams which are tapered along the length. For reasons of comparison, the planform area of the actuator is held constant and now

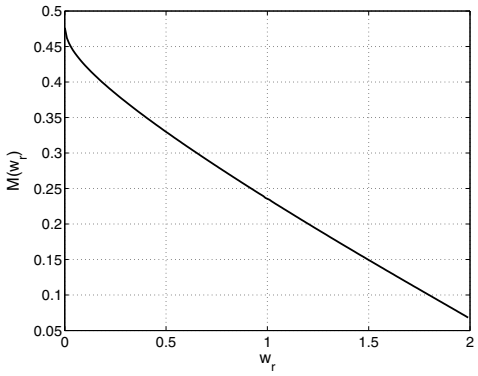

Fig. 9. $M(w_r)$ for values of w_r.

define the width as a function of x as follows:

$$w(x) = w_{\text{nom}} \left(\frac{2(1 - w_r)}{l} x + w_r \right), \tag{7}$$

where w_{nom} is the nominal width, the width at $x = l/2$, and w_r is the width ratio defined as $w_r = w_0 / w_{\text{nom}}$. Now (6) becomes:

$$m_{\text{eff}} = m_{\text{beam}} \frac{\int_0^l \dot{\delta}(x)^2 \frac{w(x)}{w_{\text{nom}}} dx}{l \dot{\delta}(l)^2}, \tag{8}$$

where now m_{beam} is $w_{\text{nom}} t l \rho$. Now $M(w_r)$ can be explicitly defined (using the displacement defined in appendix B): $M(w_r) = (g_4 + g_5 + g_6 + g_7)/g_8$ where the g_i terms are given in appendix B. This function is plotted in Fig. 9. Note that $\lim_{w_r \to 1} = 33/140$ yields the same result as for the rectangular beam.

Next, the effective mass is determined for a rectangular cantilever with a rigid extension. This is done by splitting the integral in (6) to account for the discontinuity in displacement as a function of x.

$$m_{\text{eff}} = m_{\text{beam}} \frac{\int_0^l \dot{\delta}(x)^2 \, dx + d_r \int_l^{l(1+l_r)} \dot{\delta}(x)^2 \, dx}{l(1 + d_r l_r) \dot{\delta}(l + l_{ext})^2}, \tag{9}$$

here l_r is the extension ratio equal to l_{ext}/l, m_{beam} is again the gross mass of the beam, $wl \sum \rho_b t_b (1 + l_r d_r)$ where d_r is defined as:

$$d_r = \frac{\sum_{n=1}^{N_e} \rho_e(n) t_e(n)}{\sum_{n=1}^{N_b} \rho_b(n) t_b(n)}, \tag{10}$$

where $\rho_i(n)$ and $t_i(n)$ are the density and thickness of the n^{th} layer of i^{th} section ($i \in \{b, e\}$) respectively, and N_b and N_e are the number of layers in the beam and extension. For a beam with a rigid extension, the $\delta(x)$ term is again defined in appendix B. Solving (9) yields the result shown in (11). This solution is plotted as a function of both l_r and d_r in Fig. 10. Note once again that $M(0, d_r) = 33/140$. Finally, these two results are combined to form a solution for $M(w_r, l_r, d_r)$. Again the effective mass is calculated as follows:

$$M = \frac{\int_0^l \dot{\delta}(x)^2 \frac{w(x)}{w_{\text{nom}}} dx + (2 - w_r) d_r \int_l^{l(1+l_r)} \dot{\delta}(x)^2 \, dx}{l(1 + d_r l_r (2 - w_r)) \dot{\delta}(l + l_{\text{ext}})^2}. \tag{12}$$

$$M\left(l_r, d_r\right) = \frac{33 + 7l_r\left(13 + 9l_r + 5d_r\left(4 + 3l_r\left(6 + l_r\left(11 + 2l_r\left(5 + 2l_r\right)\right)\right)\right)\right)}{140\left(1 + d_r l_r\right)\left(1 + 3l_r\left(1 + l_r\right)\right)^2} \tag{11}$$

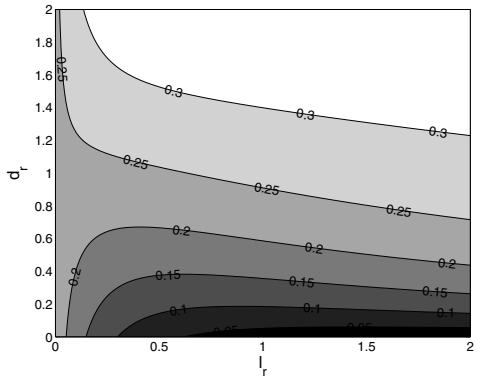

Fig. 10. $M\left(l_r, d_r\right)$ for typical ranges of l_r and d_r.

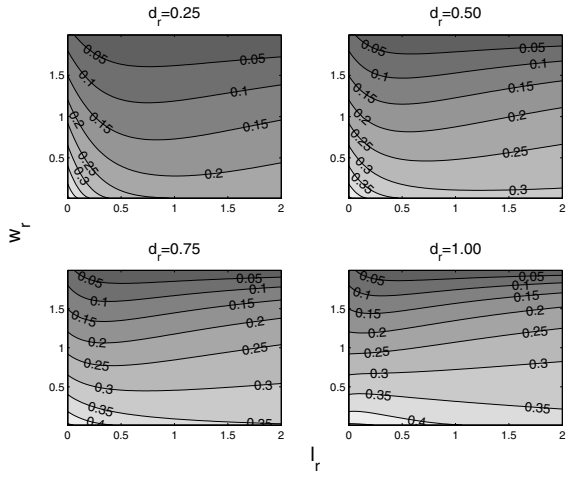

Fig. 11. $M\left(w_r, l_r, d_r\right)$ for select values of d_r.

The displacement is defined as a combination of (22) and (23) and is shown in appendix B. Substituting this into (12) yields the complete result for the effective mass of a tapered beam with a rigid extension. This result is so massive that it is not presented here for brevity, however a few level sets are shown in Fig. 11 for discrete values of d_r. Note that in all cases, the effective mass can be decreased through proper choice of geometry and material properties. This is a significant result since for a given stiffness, this will increase the actuator resonance. Thus for the same energy, this will yield higher power at the actuator resonance as well as give a higher bandwidth for control.

B. Nonlinear Stiffness

In appendix A, the actuator stiffness is derived based upon the constitutive equations for actuator performance. Now this will be re-evaluated based upon empirical observations of softening. From Wood [25], the resonant frequency of the actuator falls as a function of the peak drive field as is shown in Fig. 12. Since the effective

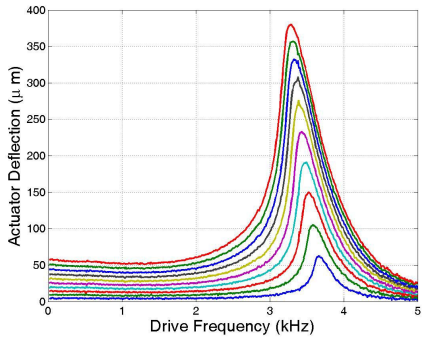

Fig. 12. Experimental magnitude frequency response for increasing field strengths (low field, $V_b = 5$ to 50V).

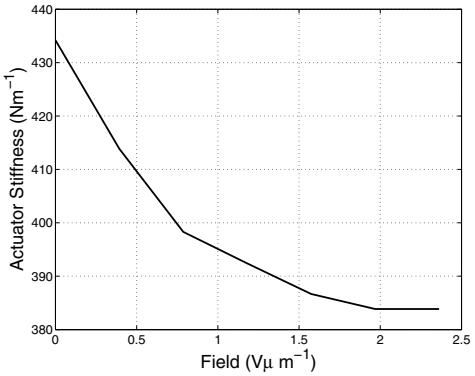

Fig. 13. Empirically measured actuator stiffness with increased field.

cantilever mass is static with respect to the applied field the resonant frequency decrease is a function of the stiffness and effective damping changing with the field. Thus highly accurate softening and loss models can be extracted by frequency sweeps, such as the one in Fig. 12, which would span the space of desired drive fields. Unfortunately, again this would fracture the actuator at high fields because of a typically high unloaded Q. Thus, to determine the stiffness as a function of applied field, static loads are applied for increasing bias field strengths and the displacement is observed. This can be done because it is assumed that there are minimal saturation effects due to an applied load, as was shown in Fig. 6. The stiffness is then extracted from this and is shown in Fig. 13.

IV. Nonconservative Parameter Modeling

All of the loss elements are lumped into the damper in Fig. 7, collectively called the actuator damping. Empirical measurements of damping for bending actuators is difficult to study since the Q of such structures is typically high so that large DC motion will result in mechanical failure (fracture) of the system at resonance. Thus, such measurements must be made at either low fields or in the presence of an external damper. Models for structure damping such as

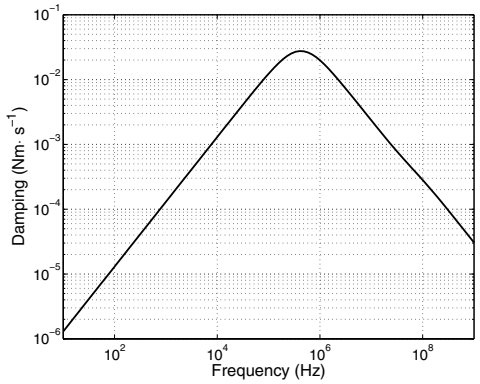

Fig. 14. Simulated frequency-dependent damping from (13).

in [5], [11] are useful for first order frequency-dependent damping approximations, however it is known that the losses for such materials increase with increasing field. To empirically verify this, static hysteresis tests are performed for increasing field strengths and the loss as a function of this field is calculated by observing how the hysteresis area changes. First, the frequency-dependent model for the loss is presented. This model is based upon the damping ratio and is given by the following:

$$b_a = 2\pi\zeta\sqrt{m_{\text{eff}}k_a}, \tag{13}$$

where ζ is the damping ratio which is related to the loss ratio $\eta = 2\zeta$ and the loss ratio (fraction of energy lost to total energy in one cycle) is defined as a transverse heat flow process in [5] by the following:

$$\eta = \frac{\alpha^2 E^Y T}{c_v}\frac{f/f_r}{1+(f/f_r)^2}. \tag{14}$$

In the above equation, α, E^Y, T, and c_v are the coefficient of thermal expansion, Young's modulus, operating temperature, and specific heat respectively while f is the operating frequency and f_r is the relaxation frequency defined in (15).

$$f_r = \frac{\pi}{2}\frac{\kappa}{c_v t_b^2}. \tag{15}$$

In the above equation for the relaxation frequency, κ is the thermal conductivity and t_b is the beam thickness. This frequency-dependent damping is simulated and shown in Fig. 14. Next, the damping as a function of the applied field is determined from the hysteresis loops shown in Fig. 15 (with no external load). From this, the loss can be measured by calculating the area in the hysteresis loop and comparing this to the total area under the curve to calculate the loss ratio (per cycle). This yields the field-dependent damping curve shown in Fig. 16.

V. Complete Model Formulation

Now all the pieces for the dynamic model are known and can be used to determine the equations of motion. Once this is complete, more interesting questions can be answered, such as actuator frequency response, power delivery capabilities, etc. The actuator model is:

$$m_{\text{eff}}\ddot{\delta} + b_a\left(f, E_3\right)\dot{\delta} + k_a\left(E_3\right)\delta = F_{\text{ext}} - F_a, \tag{16}$$

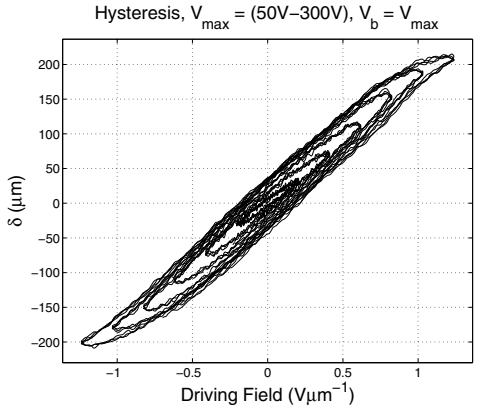

Fig. 15. Optically measured hysteresis loops for increasing fields.

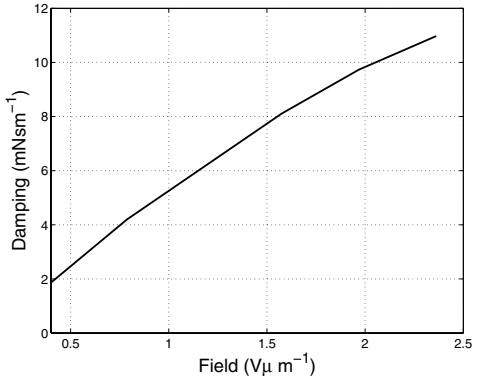

Fig. 16. Damping extracted from measured loss per cycle (extracted from Fig. 15).

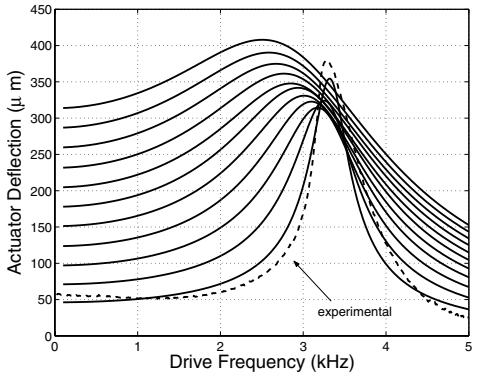

Fig. 17. Magnitude frequency response simulated from dynamic model (high fields, V_b = 50 to 300V) with 50V experimental response from Fig. 12 included.

where δ represents $\delta\left(l + l_{\text{ext}}\right)$. This model can now be used to determine the dynamic response, for example the magnitude response for various fields as is shown in Fig. 17. A few interesting points can be seen from the predicted frequency response. First, the Q degrades rapidly with increasing fields. Second, the peak displacement is a non-monotonically increasing function of the drive field. Both of these are shown in Fig. 18.

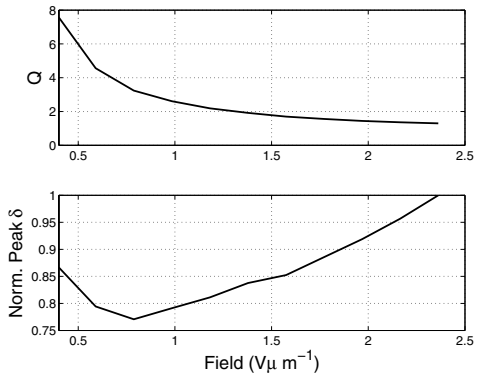

Fig. 18. Quality factor (a) and peak displacement (b) as a function of drive field (from Fig. 17).

VI. Conclusions

To calculate the power delivered to the load, it is necessary to know the load dynamics as well. For the case of a resonant system, all that is needed is the load damping b_l. The sum of the mechanical damping at the system resonance and the electromechanical damping at the drive field yields the total actuator damping. The peak power delivered to the load is given by the following:

$$P_l = \frac{1}{2}\frac{F^2 b_l}{(b_l + b_a)^2} \tag{17}$$

where F is the peak blocked force. It may appear that lowering the load damping to match the actuator losses will increase the power delivered to the load. This is not true in general since decreased load damping will increase the system Q potentially bringing the actuator closer to its strain limit at resonance. For example, with a load of $b_l = 0.1\text{Nsm}^{-1}$ (the load expected for the actuators shown in Fig. 1 for the example MAV application), the linear, low damping model predicts $> 1\text{kWkg}^{-1}$. However, when considering the effects described in this paper, this power density is reduced to approximately 800Wkg^{-1}. This places such actuators at nearly the performance of DC motors, and well above commercially available piezoelectric bending actuators.

These models and methods are of value to robotic structures because of the diverse applications and demands upon such actuators. Examples of the diverse applications which would benefit from accurate static and dynamic models are tactile displays [14], minimally invasive surgery end effectors, precision micromanipulators [15], vibration control [10], crawling robots [8] and MAVs [3].

Appendix

A. Derivations of Static Actuator Performance

In this section, a brief overview of the results obtained by Wood [25] are presented for use in further derivations. The model for quasi-static actuator performance is based upon laminate plate theory and is versatile enough to incorporate all possible combinations of piezoelectric and elastic layer layup configurations as well as intrinsic and extrinsic geometries. First, the actuator deflections are determined as a function of the geometry and internal and external excitations as follows:

$$\begin{bmatrix} \epsilon^0 \\ \kappa \end{bmatrix} = \begin{bmatrix} A_{ij} & B_{ij} \\ B_{ij} & D_{ij} \end{bmatrix}^{-1} \left(\begin{bmatrix} N_{\text{ext}} \\ M_{\text{ext}} \end{bmatrix} + \begin{bmatrix} N^p \\ M^p \end{bmatrix} \right). \tag{18}$$

In the above equation, the A_{ij}, B_{ij}, and D_{ij} terms are material and geometric constants defined in [25], $\left[\epsilon^0 \kappa\right]^T$ are the strains and curvatures, and the N and M terms are the forces and moments per unit width acting on the structure where $\left[N_{\text{ext}} M_{\text{ext}}\right]^T$ and $\left[N^p M^p\right]^T$ represent the external and piezoelectric forces and moments respectively. Of the strain terms, the curvature κ_x determines the actuator displacement since it represents the actuator curvature $d^2\delta(x)/dx^2$. Integrating this twice yields the following description of actuator motion:

$$\delta = \frac{P(E_3)\, l^2}{2} G_\delta - \frac{C_{44} F_{\text{ext}} l^3}{3 w_{\text{nom}}} G_F, \tag{19}$$

where the C matrix is the inverse of the material constant matrix in (18), $P(E_3)$ is the piezoelectric term $C_{41}N_x^p + C_{42}N_y^p + C_{44}M_x^p + C_{45}M_y^p$ and the terms G_δ and G_F are dimensionless geometric constants. The reader is urged to refer to [25] for a more detailed version of these derivations, they are only mentioned here to give an understanding of the interactions of the internal and external forces acting on the structure. Note that with no applied field, the stiffness of the actuator, k_0 is easily derived from (19):

$$k_a = \frac{3 w_{\text{nom}}}{C_{44} l^3} \frac{G_{Fb}}{G_\delta}. \tag{20}$$

B. Detail of Effective Mass Derivations

For convenience, the terms used in the derivations of the effective mass are presented here. First, the displacements due to point loads are presented. For a rectangular cantilever with no extension, the displacement is given by the following:

$$\delta(x) = -\frac{C_{44} F}{w_{\text{nom}}} \left(l\frac{x^2}{2} - \frac{x^3}{6} \right). \tag{21}$$

Now allowing for width tapering as defined in (7), the displacement if modified as follows:

$$\begin{aligned} \delta(x) = -\tfrac{C_{44} F l}{8 w_{\text{nom}} (1-w_r)^3} \big[& 2 g_1 x (g_2 l + g_1 x) \\ & + l g_2 g_3 (l w_r - 2 g_1 x) \big], \end{aligned} \tag{22}$$

where the terms $g_1 = w_r - 1$, $g_2 = w_r - 2$, and $g_3 = \ln\left[-2 g_1 x / (l w_r) + 1\right]$. Next, the displacement for a rectangular cantilever with a rigid extension is similar to (21), but split into two sections:

$$\delta(x) = \begin{cases} -\frac{C_{44} F}{w_{\text{nom}}} \left[(l + l_{\text{ext}}) \frac{x^2}{2} - \frac{x^3}{6} \right] & x : 0 \to l \\ -\frac{C_{44} F}{w_{\text{nom}}} \left[\delta_l + \alpha_l (x - l) \right] & x : l \to l + l_{\text{ext}} \end{cases}. \tag{23}$$

In (23) the terms δ_l and α_l are shorthand for $\delta(l)$ and $\left(d\delta(x)/dx\right)\big|_{x=l}$ respectively. The displacement for a beam encompassing any tapering or extension length is given in (24) (where g_9 is defined as $2 l_r g_1 + g_2$). Finally, the g_i terms used in section III-A are given in (25).

$$\delta(x) = \begin{cases} -\frac{C_{44}Fl}{8w_{\text{nom}}(1-w_r)^3}\left[2g_1x\left(lg_9+g_1x\right)+lg_3g_9\left(lw_r-2g_1x\right)\right] & x:0\rightarrow l \\ -\frac{C_{44}F}{w_{\text{nom}}}\left[\delta_l+\alpha_l\left(x-l\right)\right] & x:l\rightarrow l+l_{\text{ext}} \end{cases}. \tag{24}$$

$$\begin{aligned} g_4 &= 2g_1\left(-39624+w_r\left(135808+w_r\left(-182782+w_r\left(120878+w_r\left(-39257+4992w_r\right)\right)\right)\right)\right) \\ g_5 &= 450g_2^6\ln\left(2-w_r\right)^2 \\ g_6 &= 15g_2^4\ln\left(2-w_r\right)\left(-396+\left(676-279w_r\right)w_r-60g_2^2\ln\left(w_r\right)\right) \\ g_7 &= 15g_2^4\ln\left(w_r\right)\left(396+\left(-676+279w_r\right)w_r+30g_2^2\ln\left(w_r\right)\right) \\ g_8 &= 3600g_1\left(-6+10w_r-4w_r^2+g_2^2\ln\left(\tfrac{2-w_r}{w_r}\right)\right) \end{aligned} \tag{25}$$

ACKNOWLEDGMENTS

The authors would like to thank Srinath Avadhanula and Dr. Richard Groff for insightful discussions.

REFERENCES

[1] M. Algueró, B.L. Cheng, F. Guiu, M.J. Reece, M. Poole, and N. Alford. Degradation of the d_{33} piezoelectric coefficient for PZT under static and cyclic compressive loading. *J. of the European Ceramic Society*, 21:1437–1440, 2001.

[2] S. Avadhanula, R.J. Wood, D. Campolo, and R.S. Fearing. Dynamically tuned design of the MFI thorax. In *IEEE Intl. Conf. on Robotics and Automation*, Washington, DC, May 2002.

[3] S. Avadhanula, R.J. Wood, E. Steltz, J. Yan, and R.S. Fearing. Lift force improvements for the micromechanical flying insect. In *IEEE/RSJ Intl. Conf. on Intelligent Robots and Systems*, Las Vegas, Nevada, October 2003.

[4] D. Campolo, R. Sahai, and R.S. Fearing. Development of piezoelectric bending actuators with embedded piezoelectric sensors for micromechanical flapping mechanisms. In *IEEE Intl. Conf. on Robotics and Automation*, Taipei, Taiwan, September 2003.

[5] S.H. Crandall. The role of damping in vibration theory. *J. of Sound and Vibration*, 11(1):3–18, 1970.

[6] D. Croft, G. Shed, and S. Devasia. Creep, hysteresis, and vibration compensation for piezoactuators: Atomic force microscopy application. *J. of Dynamic Systems, Measurement, and Control*, 123:35–43, March 2001.

[7] D.L. DeVoe and A.P. Pisano. Modeling and optimal design of piezoelectric cantilever microactuators. *J. of Microelectrical Mechanical Systems*, 6(3):266–270, September 1997.

[8] M. Gogola, G. Fischer, M. Goldfarb, and E. Garcia. The development of two piezoelectrically-actuated mesoscale robot quadrupeds. In *SPIE Conf. on Microrobotics and Microassembly*, volume 3834, pages 76–84, Boston, Massachusetts, September 1999.

[9] M. Goldfarb and N. Celanovic. A lumped parameter electromechanical model for describing the nonlinear behavior of piezoelectric actuators. *Trans. of the ASME J. of Dynamic Systems, Measurement, and Control*, 119:478–485, September 1997.

[10] M.R. Kermani, M. Moallem, and R.V. Patel. Optimizing the performance of piezoelectric actuators for active vibration control. In *IEEE Intl. Conf. on Robotics and Automation*, Washington, DC, May 2002.

[11] N. Lobontiu, M. Goldfarb, and E. Garcia. Achieving maximum tip displacement during resonant excitation of piezoelectrically actuated beams. *J. of Intelligent Material Systems and Structures*, 10, November 1999.

[12] L.E. Malvern. *Introduction to the Mechanics of a Continuous Medium*. Prentice-Hall, Englewood Cliffs, NJ, 1969.

[13] S.W. Meeks and R.W. Timme. Effects of one-dimensional stress on piezoelectric ceramics. *J. of Applied Physics*, 46(10):4334–4338, October 1975.

[14] J. Pasquero and V. Hayward. STReSS: A practical tactile display system with one millimeter spatial resolution and 700hz refesh rate. In *Proc. Eurohaptics*, pages 94–110, 2003.

[15] E. Shimada, J.A. Thompson, J. Yan, R.J. Wood, and R.S. Fearing. Prototyping millirobots using dextrous microassembly and folding. In *Symp. on Microrobotics ASME Int. Mechanical Engineering Cong. and Exp.*, November 2000.

[16] U. Singh and R.S. Fearing. Tactile after-images from static contact. In 7^{th} *Symp. on Haptic Interfaces for Virtual Environment and Teleoperator Systems ASME IMECE*, Anaheim, CA, November 1998.

[17] M. Sitti, D. Campolo, J. Yan, R.S. Fearing, T. Su, D. Taylor, and T.D. Sands. Development of PZT and PZN-PT based unimorph actuators for micromechanical flapping mechanisms. In *IEEE Intl. Conf. on Robotics and Automation*, Seoul, Korea, May 2001.

[18] J.G. Smits and W. Choi. The constituent equations of piezoelectric heterogeneous bimorphs. *IEEE Trans. on Ultrasonics, Ferroelectrics, and Frequency Control*, 38(3):256–270, May 1991.

[19] E. Steltz, R.J. Wood, and R.S. Fearing. Characterization of the micromechanical flying insect by optical sensing. In *IEEE Intl. Conf. on Robotics and Automation*, Barcelona, Spain, April 2005.

[20] Q.M. Wang and L.E. Cross. Constituative equations of symmetrical triple layer piezoelectric benders. *IEEE Trans. on Ultrasonics, Ferroelectrics, and Frequency Control*, 46(6):1343–1351, November 1999.

[21] Q.M. Wang, Q. Zhang, B. Xu, R. Liu, and L.E. Cross. Nonlinear piezoelectric behavior of ceramic bending mode actuators under strong electric fields. *J. of Applied Physics*, 86(6):3352–3360, September 1999.

[22] M.S. Weinberg. Working equations for piezoelectric actuators and sensors. *J. of Microelectrical Mechanical Systems*, 8(4):529–533, December 1999.

[23] R.J. Wood, S. Avadhanula, M. Menon, and R.S. Fearing. Microrobotics using composite materials: The micromechanical flying insect thorax. In *IEEE Intl. Conf. on Robotics and Automation*, Taipei, Taiwan, September 2003.

[24] R.J. Wood and R.S. Fearing. Flight force measurements for a micromechanical flying insect. In *IEEE/RSJ Intl. Conf. on Intelligent Robots and Systems*, Maui, HI, October 2001.

[25] R.J. Wood, E. Steltz, and R.S. Fearing. Optimal energy density piezoelectric bending actuators. *To Appear: Sensors and Actuators A: Physical*, 2005.

[26] G. Yang, S.F. Liu, W. Ren, and B.K. Mukherjee. Uniaxial stress dependence of the piezoelectric properties of lead zirconate titanate ceramics. In *Proc. of the 2000 12th IEEE Intl. Symp. on Applications of Ferroelectrics*, pages 431–434, 2001.

[27] Q. M. Zhang, J. Zhao, and J. Zheng. Change of the weak-field properties of $Pb(ZrTi)O_3$ piezoceramics with compressive stresses and its links to the effect of dopants on the stability of the polarizations in the materials. *J. of Materials Research*, 12(1):226–234, 1997.